Cell Reports

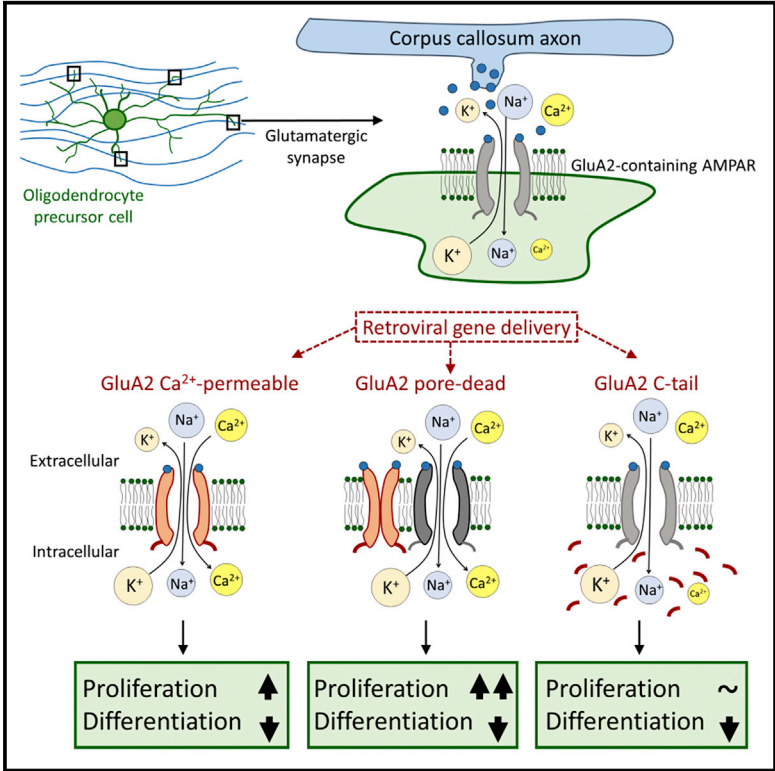# *In Vivo* Regulation of Oligodendrocyte Precursor Cell Proliferation and Differentiation by the AMPA-Receptor Subunit GluA2

Graphical Abstract

Authors

Ting-Jiun Chen, Bartosz Kula, Bálint Nagy, Ruxandra Barzan, Andrea Gall, Ingrid Ehrlich, Maria Kukley

Correspondence

maria.kukley@uni-tuebingen.de

In Brief

In the brain, oligodendrocyte precursor cells (OPCs) receive glutamatergic AMPA-receptor-mediated synaptic input from neurons. Chen et al. show that modifying AMPA-receptor properties at axon-OPC synapses alters proliferation and differentiation of OPCs. This expands the traditional view of synaptic transmission by suggesting neurons also use synapses to modulate behavior of glia.

Highlights

- AMPA receptors (AMPARs) with modified properties are expressed in OPCs *in vivo*

- Channel-pore mutations of AMPARs affect functional properties of axon-OPC synapses

- Expression of Ca^{2+}-permeable AMPARs alters proliferation and differentiation of OPCs

- Introducing the C-tail of the GluA2 subunit of AMPARs reduces differentiation of OPCs

CellPress

In Vivo Regulation of Oligodendrocyte Precursor Cell Proliferation and Differentiation by the AMPA-Receptor Subunit GluA2

Ting-Jiun Chen,[1,2] Bartosz Kula,[1,2] Bálint Nagy,[1,2,3] Ruxandra Barzan,[1,2,8] Andrea Gall,[4,5,6] Ingrid Ehrlich,[4,5,6] and Maria Kukley[1,7,9,*]

[1]Group of Neuron Glia Interaction, Werner Reichardt Centre for Integrative Neuroscience, University of Tübingen, 72076 Tübingen, Germany
[2]Graduate Training Centre of Neuroscience, University of Tübingen, 72074 Tübingen, Germany
[3]Institute of Science and Technology (IST) Austria, 3400 Klosterneuburg, Austria
[4]Learning and Memory Group, Werner Reichardt Centre for Integrative Neuroscience, University of Tübingen, 72076 Tübingen, Germany
[5]Learning and Memory Group, Hertie Institute for Brain Research, University of Tübingen, 72076 Tübingen, Germany
[6]Department of Neurobiology, IBBS, University of Stuttgart, 70569 Stuttgart, Germany
[7]Department of Ophthalmology, Research Institute of Ophthalmology, Faculty of Medicine, University Hospital Tübingen, 72076 Tübingen, Germany
[8]Present address: Optical Imaging Group, Institute for Neural Computation, Ruhr University Bochum, 44801 Bochum, Germany
[9]Lead Contact
*Correspondence: maria.kukley@uni-tuebingen.de
https://doi.org/10.1016/j.celrep.2018.09.066

SUMMARY

The functional role of AMPA receptor (AMPAR)-mediated synaptic signaling between neurons and oligodendrocyte precursor cells (OPCs) remains enigmatic. We modified the properties of AMPARs at axon-OPC synapses in the mouse corpus callosum *in vivo* during the peak of myelination by targeting the GluA2 subunit. Expression of the unedited (Ca^{2+} permeable) or the pore-dead GluA2 subunit of AMPARs triggered proliferation of OPCs and reduced their differentiation into oligodendrocytes. Expression of the cytoplasmic C-terminal (GluA2(813-862)) of the GluA2 subunit (C-tail), a modification designed to affect the interaction between GluA2 and AMPAR-binding proteins and to perturb trafficking of GluA2-containing AMPARs, decreased the differentiation of OPCs without affecting their proliferation. These findings suggest that ionotropic and non-ionotropic properties of AMPARs in OPCs, as well as specific aspects of AMPAR-mediated signaling at axon-OPC synapses in the mouse corpus callosum, are important for balancing the response of OPCs to proliferation and differentiation cues.

INTRODUCTION

In the CNS, neurons are involved in glutamatergic synaptic signaling with oligodendrocyte precursor cells (OPCs). At these neuron-glia synapses, action potentials trigger a fast vesicular release of the neurotransmitter glutamate, which binds to α-amino-3-hydroxy-5-methyl-4-isoxazolepropionic acid receptors (AMPARs) on the OPCs and leads to the activation of a depolarizing current (Bergles et al., 2000). Axon-OPC synapses are present in gray matter and white matter areas of rodent brain (Fröhlich et al., 2011) and human brain (Gallo et al., 2008), but their functional role remains a puzzle. Proliferation and differentiation of OPCs, as well as myelination, are influenced by neuronal activity (Mount and Monje, 2017). Because axon-OPC synapses represent the points of direct structural and functional interaction between the two cell types, they are ideal sites at which the effects of neuronal activity can be conveyed to glial cells. As a consequence, genetic disruption of axon-OPC synapses is expected to affect proliferation or differentiation of OPCs or myelination. However, a study showed that although permanent deletion of AMPARs in OPCs from the onset of mouse development reduced axon-OPC synaptic signaling, it did not alter proliferation and differentiation of OPCs but instead facilitated apoptotic death of oligodendrocytes (OLs) (Kougioumtzidou et al., 2017). In the present study, we used a different strategy to investigate the functional role of axon-OPC synaptic signaling: we aimed at perturbation of the properties of postsynaptic AMPARs in OPCs, rather than at perpetual deletion of these receptors.

AMPARs are large macromolecular complexes that in neurons comprise more than 30 proteins (Schwenk et al., 2014). The core of the AMPAR complex is a tetramer of GluA1–GluA4 subunits, which assemble in different combinations to form a channel pore. The GluA2 subunit is key, because it determines the single-channel conductance (Swanson et al., 1997) and the Ca^{2+} permeability of AMPARs (Hume et al., 1991). Deletion or modification of the GluA2 subunit in neurons results in strong alterations of synaptic function and animal development (Isaac et al., 2007). We expressed the full-length receptors with point mutations in the GluA2 subunit, or the truncated GluA2 subunit, in OPCs *in vivo* and assessed the effects on physiology and function of the oligodendroglial cells.
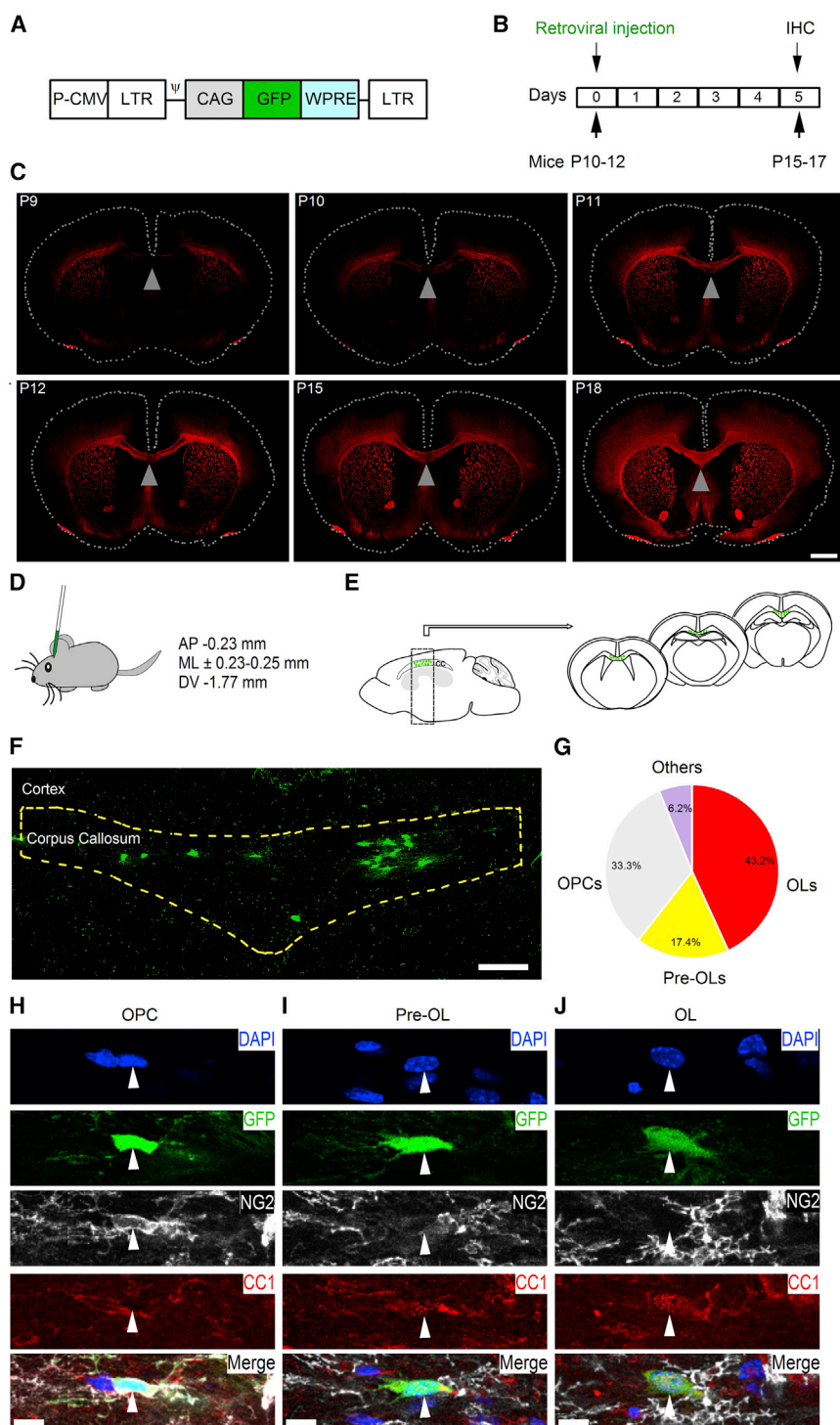
Figure 1. Retroviral Infection Specifically Targets Oligodendroglia Lineage Cells

(A) Scheme of the recombinant retroviral vector. The cytomegalovirus promoter (P-CMV) drives transcription of the viral genome; the chicken-beta actin (CAG) promoter drives expression of GFP. LTR, long terminal repeat; Ψ, viral packing signal; WPRE, Woodchuck hepatitis virus post-transcriptional regulatory element.

(B) Experimental design and timeline. IHC, immunohistochemistry.

(C) Representative images of coronal brain slices stained for myelin basic protein (red). P9, P10, P11, P12, P15, and P18 indicate postnatal days at which slices were prepared. Dashed lines indicate borders of each slice. Arrowheads point to the midline of the corpus callosum. Scale bar: 1 mm.

(D) Stereotaxic coordinates for bilateral virus injection into the corpus callosum. AP, anteroposterior; ML, mediolateral; DV, dorsoventral.

(E) Scheme showing distribution of cells infected with retrovirus (GFP$^+$ cells, green dots) in the corpus callosum. GFP$^+$ cells were found in several 300-μm-thick coronal slices along the rostro-caudal axis.

(F) Maximum intensity projection (6 successive confocal planes) showing GFP$^+$ cells in the corpus callosum (yellow dashed line). Scale bar: 100 μm.

(G) Most GFP$^+$ cells belong to the oligodendroglia lineage (n = 8 animals). OPCs, oligodendrocyte precursor cells; pre-OLs, pre-myelinating oligodendrocytes; OLs, oligodendrocytes.

(H) Maximum intensity projection (3 successive confocal planes) showing quadruple labeling for DAPI, GFP, NG2, CC1, and the merged image. The arrowhead points to an OPC (GFP$^+$NG2$^+$CC1$^-$). Stitches visible in all panels at higher magnification appeared because images have been acquired as multiple tile scans, and the edges of two neighboring tiles have not been stitched properly by the software. Scale bar: 10 μm.

(I) As in (H), but the arrowhead points to a pre-OL (GFP$^+$NG2$^+$CC1$^+$).

(J) As in (H) and (I), but the arrowhead points to an OL (GFP$^+$NG2$^-$CC1$^+$).

RESULTS

Experimental Strategies for Modifying the GluA2-Containing AMPARs in OPCs *In Vivo*

We perturbed the properties of GluA2-containing AMPARs in OPCs in the corpus callosum during the second and third post-natal weeks in mice (Figures 1A, 1B, and 2A–2C), when the OPC division rate is high (Moshrefi-Ravasdjani et al., 2017) and many OPCs differentiate into myelinating OLs, which is reflected in a steep increase of myelin basic protein expression (Figure 1C). The edited GluA2 subunit is present in callosal OPCs during this time window, because the current-voltage (I-V) relationship of AMPAR-mediated excitatory postsynaptic currents (EPSCs) in OPCs shows only slight inward rectification, with an average rectification index (RI) of 0.33 ± 0.058 (Figures S1A and S1B).

To target AMPARs specifically in OPCs, we used a retroviral gene delivery approach (Tashiro et al., 2006) and performed three manipulations (Figures 2A and 2B), which are well
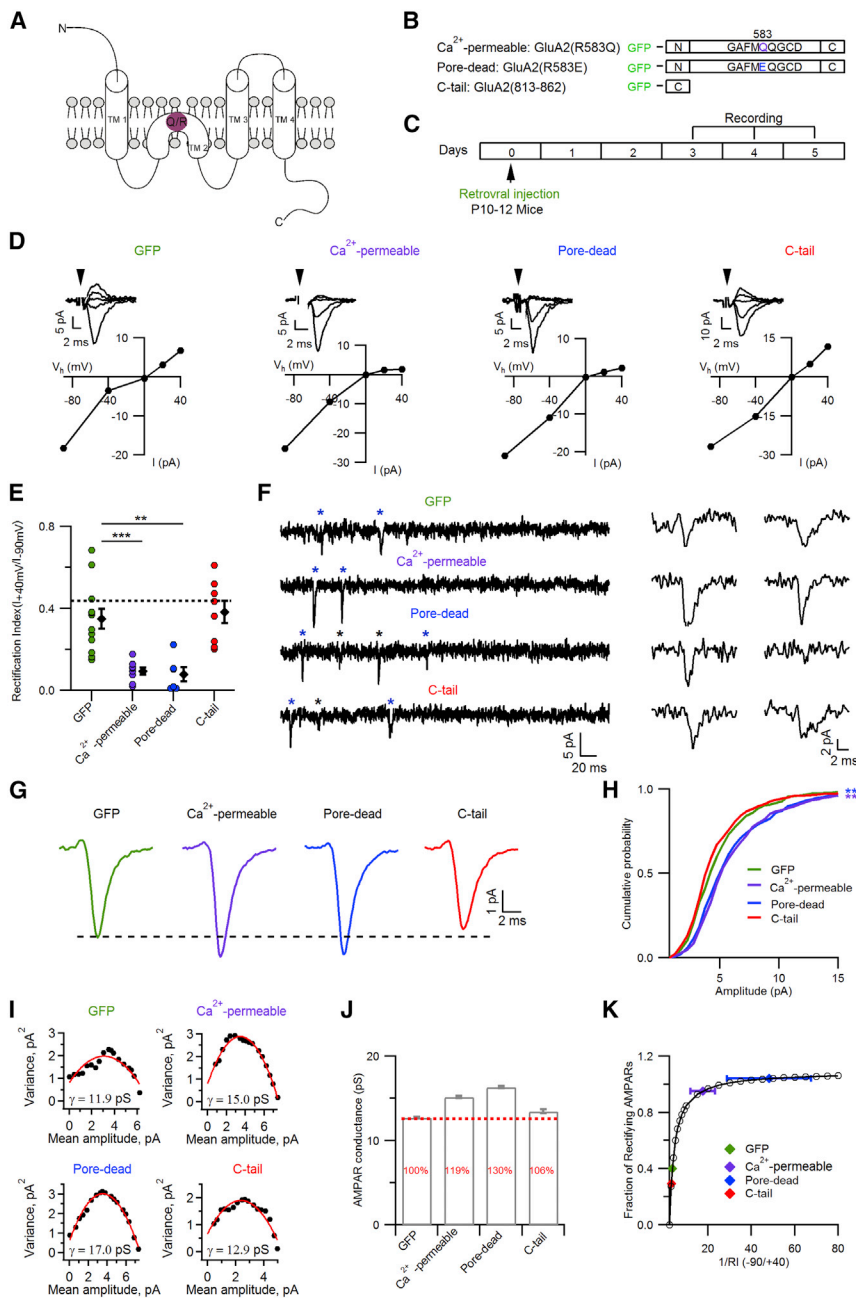
Figure 2. Modifications of the GluA2 Subunit of AMPARs in OPCs Change Rectification and Amplitude of Axon-Glia EPSCs

(A) Scheme of the GluA2 subunit of AMPARs with a Q/R editing site. Q, glutamine; R, arginine; TM, transmembrane domain; N, N terminus; C, C terminus.

(B) Scheme of the mutated and truncated GluA2 subunits fused to GFP and expressed by the viral vector. Amino acid 583 is the site of the point mutation.

(C) Experimental design and timeline for electrophysiological experiments.

(D) Examples of current-voltage (I-V) relationships of evoked EPSCs in OPCs infected with retrovirus expressing GFP or AMPAR-modifying constructs. Black dots represent the average amplitudes of 10 sweeps recorded at each holding potential (V_h). Corresponding averaged sweeps are shown above. Arrowheads indicate time of stimulation; stimulation artifacts are blanked for clarity.

(E) Rectification index (RI) for evoked EPSCs in OPCs infected with retrovirus expressing GFP (n = 12 cells/9 mice), Ca^{2+}-permeable (n = 8 cells/7 mice), pore-dead (n = 6 cells/6 mice), or C-tail (n = 8 cells/6 mice) constructs. Colored dots represent individual cells; black diamonds represent group mean ± SEM. The dashed line indicates the theoretical RI for a linear I-V relationship (0.44). One-way ANOVA (F(3, 30) = 11.800, p = 0.000028) with post hoc Games-Howell test: GFP versus Ca^{2+} permeable, ***p = 0.001; GFP versus pore dead, **p = 0.002; GFP versus C-tail, p = 0.969.

(F) Representative example traces of delayed EPSCs recorded after cessation of train stimulation in OPCs infected with retrovirus expressing GFP or AMPAR-modifying constructs (V_{hold} = −80 mV). Stars indicate delayed EPSCs; blue stars indicate events shown on the right.

(G) Averaged delayed EPSCs from OPCs expressing GFP (7 cells), Ca^{2+}-permeable (7 cells), pore-dead (8 cells), and C-tail (8 cells) constructs. In each cell, 67 events were randomly selected and averaged. Subsequently, the averages from all cells per group were pooled to generate the average EPSCs.

(H) Cumulative probability distribution of EPSC amplitudes obtained by pooling 67 randomly selected events from each cell within each experimental group. GFP, 469 events (n = 7 cells/6 mice); Ca^{2+} permeable, 469 events (n = 7 cells/6 mice); pore dead, 536 events (n = 8 cells/6 mice); C-tail, 536 events (n = 8 cells/6 mice). Kolmogorov-Smirnov test: GFP versus Ca^{2+} permeable, ***p = 0.00000013492; GFP versus pore dead, ***p = 0.000006; GFP versus C-tail, p = 0.101.

(I) Representative examples of variance-mean plots with parabola fit (red line) for delayed EPSCs recorded in OPCs expressing GFP or AMPAR-modifying constructs. The analysis is based on 85 events in each group. γ is the single-channel conductance estimated from the parabola fit.

(J) Average single-channel conductance (mean ± SEM) of synaptic AMPARs in OPCs expressing GFP or AMPAR-modifying constructs. Red numbers in the bar graphs indicate the average percentage values of single-channel conductance for different manipulations of AMPARs compared to the GFP group (100%, red dashed line).

(K) Estimation of the fraction of rectifying AMPARs (FRR) based on rectification measurements. Open circles and the black curve represent the model for measurements. Colored dots represent values of FRR corresponding to 1/RI (mean ± SEM) for GFP and AMPAR-modifying constructs.

characterized in neurons (Hayashi et al., 2000; Shi et al., 2001): (1) expression of the unedited GluA2(R583Q)-GFP subunit (Ca^{2+}-permeable), aiming to create exclusively Ca^{2+}-permeable AMPARs by replacing arginine(R)583 with glutamine(Q) (Hume et al., 1991) at the channel pore; (2) expression of the GluA2(R583E)-GFP subunit (pore-dead), aiming to reduce the number of functional GluA2-containing AMPARs by replacing arginine(R)583 with glutamic acid(E) in the channel pore

(Dingledine et al., 1992; Shi et al., 2001); and (3) overexpression of the cytoplasmic C-terminal (GluA2(813-862)) of GluA2 (C-tail), a soluble polypeptide of 50 amino acids that in neurons mediates trafficking of receptors to the membrane and interaction with other proteins within the AMPAR complex (Henley, 2003). The C-tail was expected to perturb trafficking of endogenous AMPAR in OPCs (Bassani et al., 2009; Shi et al., 2001). Each construct was tagged with GFP (Figure 2B) to identify infected cells. Recombinant retroviral vectors expressing GFP (control) (Figure 1A) or one of the constructs were stereotaxically injected into the corpus callosum of postnatal day (P) 10–P12 mice (Figures 1B and 1D).

The Retroviral Vector Specifically Targeted Oligodendroglia Lineage Cells

To verify that retroviral vectors specifically targeted OPCs, we counted oligodendroglia lineage cells positive for neuron-glia-antigen-2 (NG2) or adenomatous polyposis coli (APC/CC1) 5 days after injection of the GFP-expressing retrovirus (Figures 1E–1J). 94% of the GFP$^+$ cells were oligodendroglial cells: 33.35% ± 3.3% were GFP$^+$NG2$^+$CC1$^-$ OPCs, 17.4% ± 3.6% were GFP$^+$NG2$^+$CC1$^+$ pre-myelinating OLs (pre-OLs), and 43.2% ± 4.2% were GFP$^+$NG2$^-$CC1$^+$ mature OLs (Figures 1E–1J). Cells considered pre-OLs in our study are likely earlier pre-OLs than ENPP6$^+$ cells (Xiao et al., 2016), because the latter do not label for platelet-derived growth factor receptor alpha (PDGFRα).

Most GFP$^+$NG2$^+$ cells were not pericytes: 90% of them were located away from blood vessels and showed a rich tree of processes typical for OPCs (Bergles et al., 2000; Kukley et al., 2007), 8% were in the vicinity of a blood vessel but possessed dichotomized processes, and only 2% were near a blood vessel, had no or few processes (Figures S2A–S2G), and could be pericytes.

Thus, our retroviral vectors specifically and efficiently targeted oligodendroglia lineage cells in vivo.

Pore Mutations of the GluA2 Subunit in OPCs Changed Rectification and Amplitude of Axon-Glia EPSCs

Trafficking of full-length AMPARs to the cell surface and integration into the cell membrane are important prerequisites for their delivery to synaptic sites (Borgdorff and Choquet, 2002; Derkach et al., 2007). To verify that receptors with Ca^{2+}-permeable and pore-dead GluA2 subunits were targeted to the cell membrane of OPC, we immunolabeled the GFP fused to the N-terminal domain of the mutant GluA2 subunits (Figure S3A), without cell permeabilization (Kopec et al., 2006). GFP immunoreactivity was localized exclusively to the cell membrane and processes of OPCs (Figures S3B and S3C), confirming that mutant subunits were inserted into the membrane, from which they could be recruited to synapses by lateral diffusion. We did not assess this for the C-tail, because it is not a transmembrane protein.

To investigate changes in Ca^{2+} permeability of AMPARs at axon-OPC synapses, we studied the I-V relationship of evoked EPSCs in NG2DsRed$^+$GFP$^+$ OPCs recorded in whole-cell, voltage-clamp mode. In each experiment, we verified that the recorded cell had an electrophysiological signature of OPCs (Figure S2H) (Kukley et al., 2010) and was not a pericyte (Kawamura et al., 2002). The I-V relationship of EPSCs in OPCs expressing

the GluA2(R583Q)-GFP showed marked inward rectification (RI = 0.093 ± 0.018) (Figures 2D and 2E), as expected for Ca^{2+}-permeable AMPARs (Verdoorn et al., 1991). This suggests that modified GluA2 subunits assembled into tetrameric receptors, trafficked to the postsynaptic sites of axon-OPC synapses, and replaced the endogenous AMPARs. Clear inward rectification (RI = 0.078 ± 0.034) (Figures 2D and 2E) was also observed in OPCs expressing GluA2(R583E)-GFP, indicating that synaptic AMPARs lacked the conducting GluA2 subunit and were Ca^{2+} permeable. The expression of the C-tail did not alter the I-V relationship (RI = 0.38 ± 0.054) (Figures 2D and 2E), suggesting that the delivery of endogenous GluA2-containing AMPARs to synaptic sites was unaffected. To quantify changes of AMPAR properties, we adopted a model for estimating the fraction of rectifying Ca^{2+}-permeable receptors (Stubblefield and Benke, 2010). More than 95% of synaptic AMPARs were rectifying in OPCs expressing the Ca^{2+}-permeable or pore-dead construct, but only 40.18% ± 0.5% and 29.44% ± 0.47% were rectifying in GFP- and C-tail-expressing OPCs, respectively (Figure 2K).

To estimate alterations in the strength of individual axon-OPC synapses, we analyzed the amplitude of quantal EPSCs in OPCs (Nagy et al., 2017) (Figure 2F). The expression of Ca^{2+}-permeable and pore-dead constructs shifted the cumulative histogram toward larger current amplitudes when compared to the GFP group (Figures 2G and 2H) and increased the single-channel conductance of synaptic AMPARs (Figures 2I and 2J). A larger single-channel conductance is expected for AMPARs lacking the functional (edited) GluA2 subunit (Swanson et al., 1997), is in line with the inwardly rectifying I-V relationship (Figures 2D and 2E), and likely underlies the increase in the current amplitude. However, this result differed from that of pyramidal neurons, in which expression of the pore-dead construct reduced the EPSC amplitude (Shi et al., 2001). It is possible that in neurons, AMPARs with pore-dead GluA2 subunits merely replaced endogenous receptors, while in OPCs, the integration of pore-dead subunits was accompanied by insertion of additional functional GluA2-lacking AMPARs. Expression of the C-tail did not affect the quantal EPSC amplitude and single-channel conductance of AMPARs (Figures 2G–2J). Together with the unchanged RI (Figures 2D and 2E), this suggests that the C-tail did not alter the ionotropic function of AMPARs at axon-OPC synapses.

None of the constructs affected presynaptic properties of axon-OPC synapses, because the paired-pulse ratio (PPR) of evoked EPSCs, a parameter reflecting alterations in neurotransmitter release probability (Dobrunz and Stevens, 1997), was unchanged (Figures S3D and S3E). Retroviral infection also did not modify presynaptic release probability or the number and Ca^{2+} permeability of postsynaptic AMPARs in OPCs (Figure S1).

All Manipulations of the GluA2 Subunit Altered the Fraction of OPCs and OLs within the Oligodendroglia Lineage

To investigate changes in OPC differentiation, we counted OPCs, pre-OLs, and mature OLs labeled with specific molecular markers 5 days after the viral injection (Figures 3A–3D). The fraction of OPCs was larger in animals expressing the GluA2 subunit with pore mutations than in the GFP group (Figure 3E), while the proportion of OLs was lower (Figure 3G), suggesting
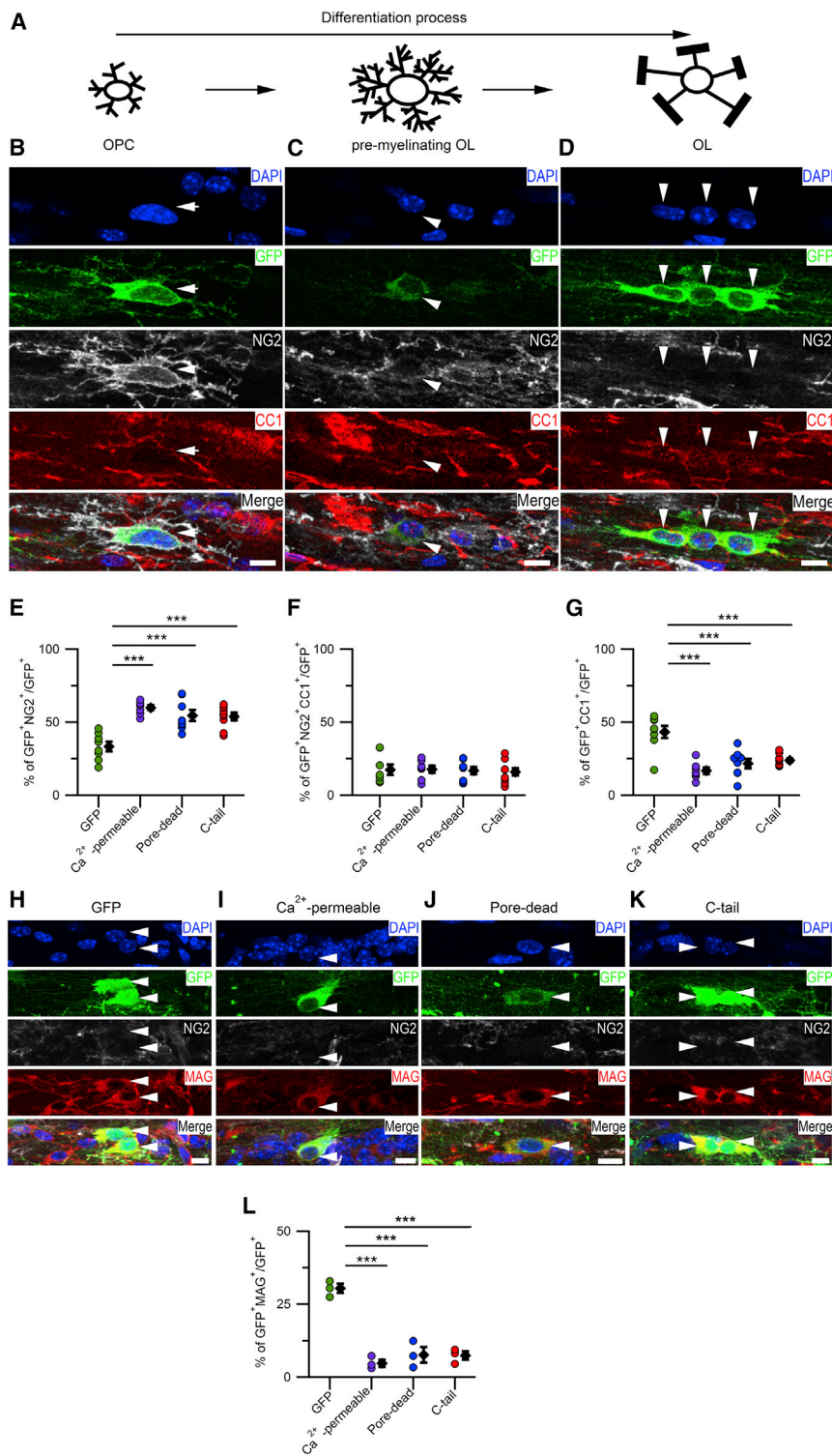
Figure 3. Modifications of the GluA2 Subunit of AMPARs in OPCs Decrease OPC Differentiation

(A) Scheme of the differentiation process in the oligodendroglia lineage.

(B) Maximum intensity projection (3 successive confocal planes) showing examples of OPC (GFP$^+$NG2$^+$CC1$^-$) infected with retrovirus expressing the pore-dead construct. Colors are as in Figures 1H–1J. Arrows point to the soma of infected cells. Scale bar: 10 μm.

(C) As in (B), but for a pre-myelinating oligodendrocyte (GFP$^+$NG2$^+$CC1$^+$).

(D) As in (B) and (C), but for an oligodendrocyte (GFP$^+$NG2$^-$CC1$^+$).

(E) Percentage of OPCs (GFP$^+$ NG2$^+$CC1$^-$) among the GFP$^+$ cells expressing GFP (n = 8), Ca^{2+}-permeable (n = 7), pore-dead (n = 8), and C-tail (n = 9) constructs. Colored dots represent individual animals; black diamonds represent group mean ± SEM. One-way ANOVA ($F_{(3, 28)}$ = 15.175, p = 0.000005) with post hoc Bonferroni test: GFP versus Ca^{2+}-permeable, ***p = 0.000008; GFP versus pore-dead, ***p = 0.000143; GFP versus C-tail, ***p = 0.000146; Ca^{2+}-permeable versus pore-dead, p = 1.000; Ca^{2+}-permeable versus C-tail, p = 1.000; pore-dead versus C-tail, p = 1.000.

(F) As in (E), but for pre-myelinating oligodendrocytes (GFP$^+$NG2$^+$CC1$^+$). One-way ANOVA ($F_{(3, 28)}$ = 0.077, p = 0.972).

(G) As in (E) and (F), but for oligodendrocytes (GFP$^+$NG2$^-$CC1$^+$). One-way ANOVA ($F_{(3, 28)}$ = 15.557, p = 0.000004) with post hoc Bonferroni test: GFP versus Ca^{2+}-permeable, ***p = 0.000006; GFP versus pore-dead, ***p = 0.000085; GFP versus C-tail, ***p = 0.000253; Ca^{2+}-permeable versus pore-dead, p = 1.000; Ca^{2+}-permeable versus C-tail, p = 0.581; pore-dead versus C-tail, p = 1.000.

(H) Maximum intensity projection (3 successive confocal planes) showing examples of MAG$^+$ oligodendrocytes (arrowheads) in an animal infected with retrovirus expressing GFP. Scale bar: 10 μm.

(I) As in (H), but for the Ca^{2+}-permeable construct.

(J) As in (H) and (I), but for the pore-dead construct.

(K) As in (H)–(J), but for the C-tail construct.

(L) Proportion of GFP$^+$NG2$^-$MAG$^+$ cells among the GFP$^+$ cells expressing GFP (n = 3 mice), Ca^{2+}-permeable (n = 3 mice), pore-dead (n = 3 mice), and C-tail (n = 3 mice) constructs. Each dot represents one animal; black diamonds represent mean ± SEM for each group. One-way ANOVA ($F_{(3, 8)}$ = 43.234, p = 0.000027) with post hoc Dunnett's test: GFP versus Ca^{2+}-permeable, ***p = 0.000023; GFP versus pore-dead, ***p = 0.000057; GFP versus C-tail, ***p = 0.000052.

that differentiation of OPCs into OLs was reduced. There was no difference in the percentage of pre-OLs between the groups (Figure 3F). The reduction in OPC differentiation was confirmed by counting the mature OLs expressing myelin-associated glycoprotein (MAG). The proportion of GFP$^+$NG2$^-$MAG$^+$ cells among GFP$^+$ cells was lower in animals expressing the GluA2 subunits with pore mutations than in the GFP group (Figures 3H–3L).

Expression of the C-tail increased the fraction of OPCs and reduced the fraction of OLs within the GFP$^+$ population (Figures 3E–3L). This was surprising, because in contrast to pore mutations, the C-tail did not alter the ionotropic function of AMPARs. It is possible that OPC differentiation was affected because the C-tail interfered with AMPAR signaling via intracellular binding partners of the GluA2 subunit.

The decrease in the fraction of OLs was not a consequence of cell death, because an apoptotic marker, activated caspase-3, was hardly detected in the corpus callosum (Figures S3F–S3K). It was also not a consequence of OPC differentiation into other cell types, because the fraction of oligodendroglia lineage cells within the GFP$^+$ population was comparable in all groups (Figures 3E–3G).

Thus, manipulations of the GluA2 subunit in callosal OPCs perturb normal differentiation of OPCs into OLs.

Pore Mutations of the GluA2-Containing AMPARs Increase Proliferation of OPCs

During the second and third postnatal weeks in mice, many OPCs are actively cycling. Therefore, an increase in the fraction of OPCs (Figure 3E) may be attributable to continued cycling of OPCs at the expense of differentiation (Figure 4A). To test this, we compared the fraction of proliferating GFP$^+$ cells in mice expressing the GFP versus mice expressing the modified GluA2 subunits, or the C-tail. We used two approaches: (1) *in vivo* labeling with 5-ethynyl-2′-deoxyuridine (EdU), which integrates during the S phase, and (2) *ex vivo* labeling for Ki67, which is present during all active phases of the cell cycle (Gerdes et al., 1984).

Pore mutations altering the Ca^{2+} permeability of AMPARs in OPCs resulted in a larger proportion of cycling cells (GFP$^+$EdU$^+$) (Figures 4B and 4C). This was caused by an increase in EdU$^+$ OPCs, because the GFP$^+$ population contained a higher percentage of NG2$^+$EdU$^+$ cells (Figure 4D). In addition, most EdU$^+$ cells were NG2$^+$ in all groups (not shown), indicating that neither of the AMPAR manipulations specifically triggered fast differentiation of EdU$^+$ OPC into OLs.

With our retroviral approach, we initially targeted cycling OPCs (Yamashita and Emerman, 2006). Therefore, the GFP$^+$ population represents cells that are progressing through or have recently completed the cell cycle. EdU injected 3–5 days after the retroviral infection incorporates only into newly synthesized DNA. Therefore, GFP$^+$EdU$^+$ cells denote cells that continued cycling, passed through the S phase again, and underwent another cell division after retroviral infection. An enhanced fraction of EdU$^+$NG2$^+$ cells within GFP$^+$ population upon alteration of Ca^{2+} permeability of AMPARs (Figure 4D) indicates that pore mutations of GluA2 subunit prompted OPCs to re-enter mitosis. If increased Ca^{2+} permeability of AMPARs triggers cell division, but does not promote differentiation, then the population of GFP$^+$NG2$^+$ cells should contain a higher proportion of EdU$^+$ cells. This was only observed for the pore-dead mutation, not the Ca^{2+}-permeable mutation (Figure 4E), suggesting that the former promoted proliferation of OPCs more effectively than the latter. In accordance with this, labeling for Ki67 on the 5th day after viral infection in animals treated with EdU (Figure 4F) showed that the proportion of still-cycling OPCs (GFP$^+$NG2$^+$ EdU$^+$Ki67$^+$) within the population of previously cycling OPCs

(GFP$^+$NG2$^+$EdU$^+$) was increased only upon expression of the pore-dead mutation (Figure 4G).

Expression of the C-tail did not alter OPC proliferation (Figures 4C–4E and 4G). Therefore, one might expect that the proportion of OPCs is lower after introducing the C-tail than after introducing the GluA2 pore mutations. But this was not the case (Figure 3E), and there was no difference in apoptotic cell death between the manipulations (Figures S3F–S3K). Two mechanisms may underlie an increase in the OPC population: (1) OPCs cycle, rather than differentiate, or (2) OPCs stay longer in the G1 phase or exit the cell cycle but do not differentiate at the usual rate (Figure 4A). When combining the data on differentiation (Figures 3E–3G) and proliferation (Figures 4C–4E and 4G) into a unified model (Figure 4H; Figure S4), we found that EdU$^+$ and EdU$^-$ OPCs contributed to increasing the population of GFP$^+$NG2$^+$ cells for all manipulations (Figure 4H). However, for the pore-dead construct, the fraction of EdU$^+$ OPCs was higher than the fraction of EdU$^-$ OPCs; for the C-tail, the opposite was true; and for the Ca^{2+}-permeable construct, the contribution of those two populations was roughly equal (Figure 4H). This indicates that both mechanisms play a role but that their impact is different depending on the properties of AMPARs. Therefore, axon-OPC synapses are likely involved in regulating the ratio between cycling and non-cycling OPCs.

DISCUSSION

Our major finding is that manipulating the key properties of AMPARs at axon-OPC synapses *in vivo* at the peak of myelination results in altered balance between proliferation and differentiation of OPCs.

In cell culture, AMPARs regulate proliferation and differentiation of OPCs (Fannon et al., 2015; Gallo et al., 1996; Hossain et al., 2014; Yuan et al., 1998), and Ca^{2+}-permeable AMPARs indirectly modulate the expression of genes involved in differentiation and growth (Pende et al., 1994). Ca^{2+} ions are important modulators of proliferation and differentiation of many cells, including neuronal progenitors and tumor and endothelial cells (Cui et al., 2017; Jansson and Åkerman, 2014; Moccia et al., 2012). Our findings *in vivo* suggest that Ca^{2+} permeability of AMPARs may be a key mechanism modulating the development of oligodendroglial cells. During the second and third postnatal weeks in mice, when extensive myelination of axons takes place, OPCs efficiently respond to proliferation and differentiation cues, but it is unknown how OPCs make the choice between the two processes. In GFP controls and in non-injected mice, the RI was highly variable, ranging from 0.15 to 0.68 (Figure 2E; Figure S1B). Hence, during normal development, some OPCs have higher Ca^{2+} permeability of AMPARs than others. Possibly, OPCs with high Ca^{2+} permeability of AMPARs continue cycling, while OPCs with low Ca^{2+} permeability of AMPARs are prone to differentiate. This is also suggested by a study showing that AMPARs in differentiating OPCs have lower Ca^{2+} permeability than immature OPCs (Zonouzi et al., 2011). Thus, Ca^{2+} permeability of AMPARs is likely a physiological mechanism regulating the choice between proliferation and differentiation of OPCs. Another mechanism may be the subunit composition of AMPARs. We found that the pore-dead mutation of the GluA2
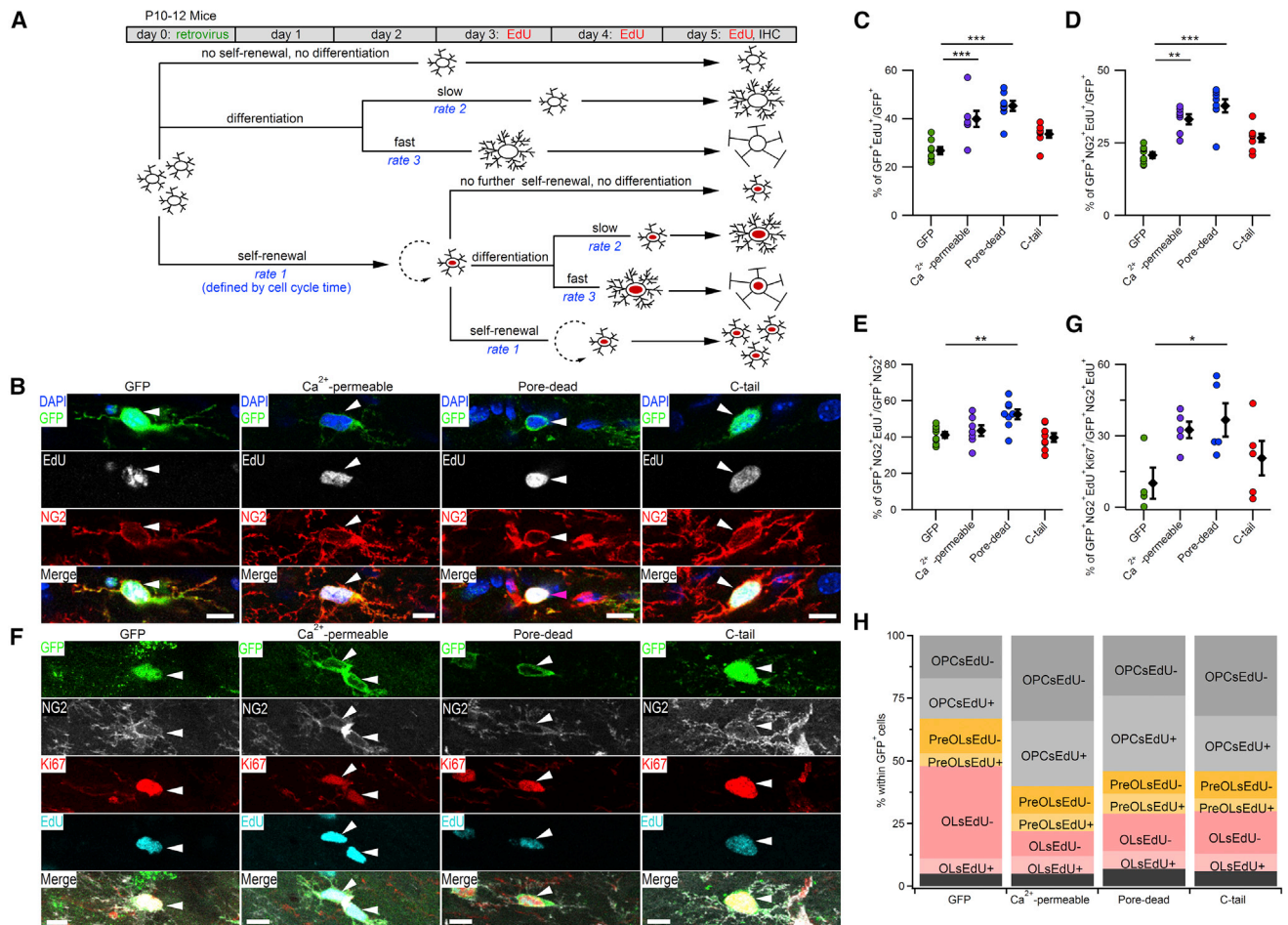
Figure 4. Modifications Rendering AMPARs Ca^{2+} Permeable Increase OPC Proliferation

(A) Scheme illustrating that OPCs infected with retrovirus can follow different developmental fates. Cells with a red nucleus indicate EdU$^+$ cells. IHC, immunohistochemistry.

(B) Maximum intensity projection (2 successive confocal planes) showing examples of quadruple labeling for DAPI (blue), GFP (green), EdU (white), and NG2 (red) and a merged image in animals expressing the GFP, Ca^{2+}-permeable, pore-dead, or C-tail construct. White arrowheads mark GFP$^+$NG2$^+$EdU$^+$ cells. Scale bar: 10 μm.

(C) Proportion of GFP$^+$EdU$^+$ cells among the GFP$^+$ cells expressing the GFP (n = 8 mice), Ca^{2+}-permeable (n = 7 mice), pore-dead (n = 8 mice), and C-tail (n = 8 mice) constructs. Colored dots represent individual animals; black diamonds represent group mean ± SEM. One-way ANOVA (F(3, 27) = 14.234, p = 0.000009) with post hoc Dunnett's test: GFP versus Ca^{2+}-permeable, ***p = 0.001; GFP versus pore-dead, ***p = 0.000004; GFP versus C-tail, p = 0.074.

(D) As in (C), but for the proportion of GFP$^+$NG2$^+$EdU$^+$ among the GFP$^+$ cells. Kruskal-Wallis test (H(3) = 21.277, p = 0.000092) with post hoc Dunn's test: GFP versus Ca^{2+}-permeable, **p = 0.009; GFP versus pore-dead, ***p = 0.000084; GFP versus C-tail, p = 0.499.

(E) As in (C) and (D), but for the proportion of GFP$^+$NG2$^+$EdU$^+$ cells among the GFP$^+$NG2$^+$ cells. One-way ANOVA (F(3, 27) = 5.569, p = 0.004) with post hoc Dunnett's test: GFP versus Ca^{2+}-permeable, p = 0.838; GFP versus pore-dead, *p = 0.007; GFP versus C-tail, p = 0.985.

(F) Maximum intensity projection (3 successive confocal planes) showing examples of quadruple labeling for GFP (green), NG2 (white), Ki67 (red), and EdU (cyan) and a merged image in animals expressing GFP or AMPAR-modifying constructs. The arrowheads point to infected Ki67$^+$EdU$^+$ OPC (GFP$^+$NG2$^+$EdU$^+$Ki67$^+$). Scale bar: 10 μm.

(G) Proportion of GFP$^+$NG2$^+$EdU$^+$ cells labeled for Ki67 among the GFP$^+$ cells expressing the GFP (n = 4 mice), Ca^{2+}-permeable (n = 5 mice), pore-dead (n = 5 mice), or C-tail (n = 5 mice) constructs. Each dot represents one animal; black diamonds represent mean ± SEM for each group. One-way ANOVA (F(3, 15) = 3.47, p = 0.043) with post hoc Dunnett's test: GFP versus Ca^{2+}-permeable, p = 0.067, GFP versus pore-dead, *p = 0.027, GFP versus C-tail, p = 0.53.

(H) Cumulative bar graphs showing all subpopulations of cells comprising the GFP$^+$ population. Calculations are derived from all data on proliferation and differentiation and are specified in Figure S4. Colored bars indicate oligodendrocyte linage cells; black bars indicate other cells.

subunit triggered stronger changes in OPC proliferation than the Ca^{2+}-permeable mutation (Figures 4E and 4G), although electrophysiological changes at axon-OPC synapses were similar (Figures 2D–2K). An important difference between the pore-dead and the Ca^{2+}-permeable mutations is that ionic conductance is carried only by GluA2-lacking AMPARs in the former case but by AMPARs composed of all subunits (including the unedited GluA2) in the latter case. The downstream signaling cascades may differ depending on the subunit composition, resulting in distinct regulatory mechanisms of the OPC cell cycle.

Regulation of OPC differentiation may also involve the non-ionotropic function of AMPARs, because expression of the C-tail did not alter the AMPAR ionotropic function but did reduce differentiation. AMPAR subunits interact with various binding proteins, including GRIP, TARP, PICK, ABP, SAP97, NSF, and the PLP-integrin-G_i complex (Harlow et al., 2015; Henley, 2003; Henley and Wilkinson, 2016), and many of these interactions involve the cytoplasmic C-tails of AMPAR subunits (Henley, 2003). Expression of the C-tail may have perturbed some of these interactions, for instance, interaction between AMPARs and integrins, which play a key role for differentiation of the oligodendroglial cells (Baron et al., 2005). It will be important to investigate the interaction partners of the GluA2 C-tail in OPCs and to use pharmacological and genetic approaches to identifying the molecular cascades inducing changes in OPC differentiation by non-ionotropic mechanisms.

Proliferation and differentiation of OPCs can be modulated by neuronal activity (Mount and Monje, 2017), and some patterns of activity are more likely to promote proliferation, while others are more likely to promote differentiation (Nagy et al., 2017). Synaptic AMPARs in OPCs are good candidates to transduce the effects of neuronal activity to OPCs. Our findings that different manipulations of AMPARs *in vivo* result in distinct changes in proliferation and differentiation suggest that even the same pattern of neuronal activity may affect OPCs differently depending on the subunit composition of postsynaptic AMPARs in OPCs.

Our manipulations of the established AMPAR signaling in OPCs had a different outcome than elimination of AMPARs from the onset of mouse development (Kougioumtzidou et al., 2017). Proliferation and differentiation of OPCs is likely controlled via several signaling pathways (Huang et al., 2013), with AMPAR signaling being one of them. Germline deletion of AMPARs in OPCs may trigger compensatory mechanisms, resulting in normal proliferation and lineage progression of OPCs in the postnatal brain (Kougioumtzidou et al., 2017). This is less likely in our study, because we induced acute alterations at axon-OPC synapses. Another difference is that we specifically targeted and analyzed the dividing OPCs, while Kougioumtzidou et al. (2017) investigated the entire population of OPCs (cycling OPCs and cells in the G0 phase). AMPAR signaling may play a more prominent role in proliferating OPCs, which have to transfer synaptic contacts to their daughter cells (Ge et al., 2009; Kukley et al., 2008), making the effects of AMPAR modifications more evident in these cells.

Our findings have important implications for future research on the properties and function of AMPARs in OPCs during diseases. Injury triggers trafficking of GluA2-lacking (Ca^{2+}-permeable) AMPARs to the membrane in neurons, and this process can be initiated by inflammatory molecules (Yin et al., 2012). Similar events may take place in OPCs during inflammatory demyelination, spinal cord injury, and other pathological conditions. Therefore, investigating and manipulating properties and downstream signaling of AMPARs in OPCs during diseases is important for opening new therapeutic avenues.

STAR★METHODS

Detailed methods are provided in the online version of this paper and include the following:

SUPPLEMENTAL INFORMATION

Supplemental Information includes four figures and can be found with this article online at https://doi.org/10.1016/j.celrep.2018.09.066.

AUTHOR CONTRIBUTIONS

Conceptualization, T.-J.C., I.E., and M.K.; Methodology, T.-J.C., B.K., B.N., A.G., I.E., and M.K.; Software, M.K.; Validation, T.-J.C., B.K., B.N., R.B., and M.K.; Formal Analysis, T.-J.C., B.K., B.N., and M.K.; Investigation, T.-J.C., B.K., B.N., R.B., and M.K.; Writing – Original Draft, T.-J.C., I.E., and M.K.; Writing – Review & Editing, T.-J.C., B.K., B.N., R.B., I.E., and M.K.; Visualization, T.-J.C. and M.K.; Supervision, I.E. and M.K.; Funding Acquisition, I.E. and M.K.

REFERENCES

Baron, W., Colognato, H., and Ffrench-Constant, C. (2005). Integrin-growth factor interactions as regulators of oligodendroglial development and function. Glia *49*, 467–479.

Bassani, S., Valnegri, P., Beretta, F., and Passafaro, M. (2009). The GLUR2 subunit of AMPA receptors: synaptic role. Neuroscience *158*, 55–61.

Bergles, D.E., Roberts, J.D., Somogyi, P., and Jahr, C.E. (2000). Glutamatergic synapses on oligodendrocyte precursor cells in the hippocampus. Nature *405*, 187–191.

Borgdorff, A.J., and Choquet, D. (2002). Regulation of AMPA receptor lateral movements. Nature *417*, 649–653.

Cui, C., Merritt, R., Fu, L., and Pan, Z. (2017). Targeting calcium signaling in cancer therapy. Acta Pharm. Sin. B *7*, 3–17.

Derkach, V.A., Oh, M.C., Guire, E.S., and Soderling, T.R. (2007). Regulatory mechanisms of AMPA receptors in synaptic plasticity. Nat. Rev. Neurosci. *8*, 101–113.

Dingledine, R., Hume, R.I., and Heinemann, S.F. (1992). Structural determinants of barium permeation and rectification in non-NMDA glutamate receptor channels. J. Neurosci *12*, 4080–4087.

Dobrunz, L.E., and Stevens, C.F. (1997). Heterogeneity of release probability, facilitation, and depletion at central synapses. Neuron *18*, 995–1008.

Fannon, J., Tarmier, W., and Fulton, D. (2015). Neuronal activity and AMPA-type glutamate receptor activation regulates the morphological development of oligodendrocyte precursor cells. Glia *63*, 1021–1035.

Fröhlich, N., Nagy, B., Hovhannisyan, A., and Kukley, M. (2011). Fate of neuron-glia synapses during proliferation and differentiation of NG2 cells. J. Anat. *219*, 18–32.

Gallo, V., Zhou, J.M., McBain, C.J., Wright, P., Knutson, P.L., and Armstrong, R.C. (1996). Oligodendrocyte progenitor cell proliferation and lineage progression are regulated by glutamate receptor-mediated K+ channel block. J. Neurosci. *16*, 2659–2670.

Gallo, V., Mangin, J.M., Kukley, M., and Dietrich, D. (2008). Synapses on NG2-expressing progenitors in the brain: multiple functions? J. Physiol. *586*, 3767–3781.

Ge, W.P., Zhou, W., Luo, Q., Jan, L.Y., and Jan, Y.N. (2009). Dividing glial cells maintain differentiated properties including complex morphology and functional synapses. Proc. Natl. Acad. Sci. USA *106*, 328–333.

Gerdes, J., Lemke, H., Baisch, H., Wacker, H.H., Schwab, U., and Stein, H. (1984). Cell cycle analysis of a cell proliferation-associated human nuclear antigen defined by the monoclonal antibody Ki-67. J. Immunol. *133*, 1710–1715.

Harlow, D.E., Saul, K.E., Komuro, H., and Macklin, W.B. (2015). Myelin proteolipid protein complexes with αv integrin and AMPA receptors *in vivo* and regulates AMPA-dependent oligodendrocyte progenitor cell migration through the modulation of cell-surface GluR2 expression. J. Neurosci. *35*, 12018–12032.

Hartveit, E., and Veruki, M.L. (2007). Studying properties of neurotransmitter receptors by non-stationary noise analysis of spontaneous postsynaptic currents and agonist-evoked responses in outside-out patches. Nat. Protoc. *2*, 434–448.

Hayashi, Y., Shi, S.H., Esteban, J.A., Piccini, A., Poncer, J.C., and Malinow, R. (2000). Driving AMPA receptors into synapses by LTP and CaMKII: requirement for GluR1 and PDZ domain interaction. Science *287*, 2262–2267.

Henley, J.M. (2003). Proteins interactions implicated in AMPA receptor trafficking: a clear destination and an improving route map. Neurosci. Res. *45*, 243–254.

Henley, J.M., and Wilkinson, K.A. (2016). Synaptic AMPA receptor composition in development, plasticity and disease. Nat. Rev. Neurosci. *17*, 337–350.

Hossain, S., Liu, H.N., Fragoso, G., and Almazan, G. (2014). Agonist-induced down-regulation of AMPA receptors in oligodendrocyte progenitors. Neuropharmacology *79*, 506–514.

Huang, H., Zhao, X.F., Zheng, K., and Qiu, M. (2013). Regulation of the timing of oligodendrocyte differentiation: mechanisms and perspectives. Neurosci. Bull. *29*, 155–164.

Hume, R.I., Dingledine, R., and Heinemann, S.F. (1991). Identification of a site in glutamate receptor subunits that controls calcium permeability. Science *253*, 1028–1031.

Isaac, J.T., Ashby, M.C., and McBain, C.J. (2007). The role of the GluR2 subunit in AMPA receptor function and synaptic plasticity. Neuron *54*, 859–871.

Jansson, L.C., and Åkerman, K.E. (2014). The role of glutamate and its receptors in the proliferation, migration, differentiation and survival of neural progenitor cells. J. Neural Transm. (Vienna) *121*, 819–836.

Kawamura, H., Oku, H., Li, Q., Sakagami, K., and Puro, D.G. (2002). Endothelin-induced changes in the physiology of retinal pericytes. Invest. Ophthalmol. Vis. Sci. *43*, 882–888.

Kopec, C.D., Li, B., Wei, W., Boehm, J., and Malinow, R. (2006). Glutamate receptor exocytosis and spine enlargement during chemically induced long-term potentiation. J. Neurosci. *26*, 2000–2009.

Kougioumtzidou, E., Shimizu, T., Hamilton, N.B., Tohyama, K., Sprengel, R., Monyer, H., Attwell, D., and Richardson, W.D. (2017). Signalling through AMPA receptors on oligodendrocyte precursors promotes myelination by enhancing oligodendrocyte survival. eLife *6*, e28080.

Kukley, M., Capetillo-Zarate, E., and Dietrich, D. (2007). Vesicular glutamate release from axons in white matter. Nat. Neurosci. *10*, 311–320.

Kukley, M., Kiladze, M., Tognatta, R., Hans, M., Swandulla, D., Schramm, J., and Dietrich, D. (2008). Glial cells are born with synapses. FASEB J. *22*, 2957–2969.

Kukley, M., Nishiyama, A., and Dietrich, D. (2010). The fate of synaptic input to NG2 glial cells: neurons specifically downregulate transmitter release onto differentiating oligodendroglial cells. J. Neurosci. *30*, 8320–8331.

Moccia, F., Dragoni, S., Lodola, F., Bonetti, E., Bottino, C., Guerra, G., Laforenza, U., Rosti, V., and Tanzi, F. (2012). Store-dependent Ca(2+) entry in endothelial progenitor cells as a perspective tool to enhance cell-based therapy and adverse tumour vascularization. Curr. Med. Chem. *19*, 5802–5818.

Moshrefi-Ravasdjani, B., Dublin, P., Seifert, G., Jennissen, K., Steinhäuser, C., Kafitz, K.W., and Rose, C.R. (2017). Changes in the proliferative capacity of NG2 cell subpopulations during postnatal development of the mouse hippocampus. Brain Struct. Funct. *222*, 831–847.

Mount, C.W., and Monje, M. (2017). Wrapped to adapt: experience-dependent myelination. Neuron *95*, 743–756.

Nagy, B., Hovhannisyan, A., Barzan, R., Chen, T.J., and Kukley, M. (2017). Different patterns of neuronal activity trigger distinct responses of oligodendrocyte precursor cells in the corpus callosum. PLoS Biol. *15*, e2001993.

Pende, M., Holtzclaw, L.A., Curtis, J.L., Russell, J.T., and Gallo, V. (1994). Glutamate regulates intracellular calcium and gene expression in oligodendrocyte progenitors through the activation of DL-alpha-amino-3-hydroxy-5-methyl-4-isoxazolepropionic acid receptors. Proc. Natl. Acad. Sci. USA *91*, 3215–3219.

Pernía-Andrade, A.J., Goswami, S.P., Stickler, Y., Fröbe, U., Schlögl, A., and Jonas, P. (2012). A deconvolution-based method with high sensitivity and temporal resolution for detection of spontaneous synaptic currents *in vitro* and *in vivo*. Biophys. J. *103*, 1429–1439.

Rozov, A., Zilberter, Y., Wollmuth, L.P., and Burnashev, N. (1998). Facilitation of currents through rat Ca2+-permeable AMPA receptor channels by activity-dependent relief from polyamine block. J. Physiol. *511*, 361–377.

Schwenk, J., Baehrens, D., Haupt, A., Bildl, W., Boudkkazi, S., Roeper, J., Fakler, B., and Schulte, U. (2014). Regional diversity and developmental dynamics of the AMPA-receptor proteome in the mammalian brain. Neuron *84*, 41–54.

Shi, S., Hayashi, Y., Esteban, J.A., and Malinow, R. (2001). Subunit-specific rules governing AMPA receptor trafficking to synapses in hippocampal pyramidal neurons. Cell *105*, 331–343.

Stubblefield, E.A., and Benke, T.A. (2010). Distinct AMPA-type glutamatergic synapses in developing rat CA1 hippocampus. J. Neurophysiol. *104*, 1899–1912.

Swanson, G.T., Kamboj, S.K., and Cull-Candy, S.G. (1997). Single-channel properties of recombinant AMPA receptors depend on RNA editing, splice variation, and subunit composition. J. Neurosci. *17*, 58–69.

Tashiro, A., Zhao, C., and Gage, F.H. (2006). Retrovirus-mediated single-cell gene knockout technique in adult newborn neurons *in vivo*. Nat. Protoc. *1*, 3049–3055.

Verdoorn, T.A., Burnashev, N., Monyer, H., Seeburg, P.H., and Sakmann, B. (1991). Structural determinants of ion flow through recombinant glutamate receptor channels. Science 252, 1715–1718.

Xiao, L., Ohayon, D., McKenzie, I.A., Sinclair-Wilson, A., Wright, J.L., Fudge, A.D., Emery, B., Li, H., and Richardson, W.D. (2016). Rapid production of new oligodendrocytes is required in the earliest stages of motor-skill learning. Nat. Neurosci. 19, 1210–1217.

Yamashita, M., and Emerman, M. (2006). Retroviral infection of non-dividing cells: old and new perspectives. Virology 344, 88–93.

Yin, H.Z., Hsu, C.I., Yu, S., Rao, S.D., Sorkin, L.S., and Weiss, J.H. (2012). TNF-α triggers rapid membrane insertion of Ca(2+) permeable AMPA receptors into adult motor neurons and enhances their susceptibility to slow excitotoxic injury. Exp. Neurol. 238, 93–102.

Young, K.M., Psachoulia, K., Tripathi, R.B., Dunn, S.J., Cossell, L., Attwell, D., Tohyama, K., and Richardson, W.D. (2013). Oligodendrocyte dynamics in the healthy adult CNS: evidence for myelin remodeling. Neuron 77, 873–885.

Yuan, X., Eisen, A.M., McBain, C.J., and Gallo, V. (1998). A role for glutamate and its receptors in the regulation of oligodendrocyte development in cerebellar tissue slices. Development 125, 2901–2914.

Ziskin, J.L., Nishiyama, A., Rubio, M., Fukaya, M., and Bergles, D.E. (2007). Vesicular release of glutamate from unmyelinated axons in white matter. Nat. Neurosci. 10, 321–330.

Zonouzi, M., Renzi, M., Farrant, M., and Cull-Candy, S.G. (2011). Bidirectional plasticity of calcium-permeable AMPA receptors in oligodendrocyte lineage cells. Nat. Neurosci. 14, 1430–1438.

STAR★METHODS

KEY RESOURCES TABLE

REAGENT or RESOURCE	SOURCE	IDENTIFIER
Antibodies		
Guinea pig anti-NG2 Antibody	William Stallcup, Sanford Burnham Prebys Medical Discovery Institute, USA	Cat# Anti-NG2, RRID:AB_2572299
Rabbit anti-NG2 Antibody	William Stallcup,Sanford Burnham Prebys Medical Discovery Institute, USA	Cat# NG2-rabbit, RRID:AB_2572298
Anti-APC (Ab-7) Mouse mAb (CC-1) antibody	Millipore	Cat# OP80, RRID:AB_2057371
Cleaved Caspase-3 (Asp175) (5A1E) Rabbit mAb antibody	Cell Signaling Technology	Cat# 9664, RRID:AB_2070042
Anti-GFP Antibody	Abcam	Cat# ab13970, RRID:AB_300798
Rat Anti-Myelin Basic Protein Monoclonal Antibody, Unconjugated, Clone 12	Abcam	Cat# ab7349, RRID:AB_305869
Mouse Anti-Ki-67 Monoclonal Antibody, Unconjugated, Clone B56	BD Biosciences	Cat# 556003, RRID:AB_396287
Mouse Anti-MAG Monoclonal Antibody, Unconjugated	Santa Cruz Biotechnology	Cat# sc-166849, RRID:AB_2250078
Goat anti-Rabbit IgG (H+L) Cross-Adsorbed Secondary Antibody, Alexa Fluor 568	Thermo Fisher Scientific	Cat# A-11011, RRID:AB_143157
Cy5 antibody	Jackson ImmunoResearch Labs	Cat# 111-175-003, RRID:AB_2314269
Goat anti-Rabbit IgG (H+L) Secondary Antibody, Alexa Fluor 405	Thermo Fisher Scientific	Cat# A-31556, RRID:AB_221605
Goat anti-Guinea Pig IgG (H+L) Highly Cross-Adsorbed Secondary Antibody, Alexa Fluor 633	Thermo Fisher Scientific	Cat# A-21105, RRID:AB_2535757
Goat anti-Mouse IgG (H+L) Secondary Antibody, Alexa Fluor 555 conjugate	Thermo Fisher Scientific	Cat# A-21422, RRID:AB_2535844
Fluorescein (FITC)-AffiniPure Donkey Anti-Chicken IgY (IgG) (H+L) (min X Bov,Gt,GP,Sy Hms,Hrs,Hu,Ms,Rb,Rat,Shp Sr Prot) antibody	Jackson ImmunoResearch Labs	Cat# 703-095-155, RRID:AB_2340356
Goat anti-Chicken IgY (H+L) Secondary Antibody, Alexa Fluor 488	Thermo Fisher Scientific	Cat# A-11039, RRID:AB_2534096
Biotin-SP-AffiniPure Goat Anti-Rat IgG (H+L) antibody	Jackson ImmunoResearch Labs	Cat# 112-065-003, RRID:AB_2338168
Cy3-Streptavidin antibody	Jackson ImmunoResearch Labs	Cat# 016-160-084, RRID:AB_2337244
Bacterial and Virus Strains		
XL 10-Gold ultracompetent cells	Stratagene	Cat# 200521
Stbl3 competent cells	ThermoFisher	Cat#C73730
Chemicals, Peptides, and Recombinant Proteins		
Diamidino-2-phenylindole dihydrochloride (DAPI)	Sigma-Aldrich	Cat# D954
Spermine tetrachydrocloride	Sigma-Aldrich	Cat# 1141
(RS)-CPP	Tocris Bioscience	Cat# 0173
Gabazine	Abcam	Cat# ab120042
Tetrodotoxin citrate	Abcam	Cat# ab120055
CNQX disodium salt	Abcam	Cat# ab120044
Cesium methanesulfonate	Sigma-Aldrich	Cat# C1426
Tetraethylammonium (TEA) Chloride	Sigma-Aldrich	Cat# T2265
Experimental Models: Cell Lines		
HEK293T/17	ATCC	Cat# CRL-11268, RRID:CVCL_1926

Continued

REAGENT or RESOURCE	SOURCE	IDENTIFIER
Experimental Models: Organisms/Strains		
STOCK Tg(Cspg4-DsRed.T1)1Akik/J	The Jackson Laboratory	RRID:IMSR_JAX:008241
C57BL/6	Charles River Laboratories	Strain Code: 027
Oligonucleotides		
Primers for mutagenesis: Fwd: CTTGGGTGCCTTTATGGAGCAGGGATGCGATATTTC Rev: GAAATATCGCATCCCTGCTCCATAAAGGCACCCAAG	Eurofins	N/A
Primers for cloning of EGFPGluA2(R583Q) and EGFPGluA2(R583E): Fwd: TTACCGGTACGACTCACTATAGGCTAGAACTAG Rev: TGTTTAAACCCAAGGCCTGCATGCACTGCTTTG	Eurofins	N/A
Primers for cloning of EGFPGluA2(813-862) Fwd: TAGCGCT ACCGGT CGCCACCATGGTG Rev: TGGTTTAAACACCTCTACAAATGTGGTATGGCTG	Eurofins	N/A
Primers for sequencing of pRetroCAG-EGFPGluA2(R683Q) and pRetroCAG-EGFPGluA2(R683E) Fwd: CTGACATTGCAATTGCTCC Rev: ACGTTGCTCAGACTGAG	Eurofins	N/A
Primers for sequencing of pRetroCAG-EGFPGluA2(813-862) Fwd: TCACATGGTCCTGCTGG Fwd: ATCGACTTCAAGGAGGAC	Eurofins	N/A
Recombinant DNA		
pCI-EGFPGluA2(R583Q)	Roberto Malinow, University of California, USA	N/A
pEGFPC1-GluA2(813-862)	Ingrid Ehrlich, University of Tuebingen and University of Stuttgart, Germany	N/A
pRetroCAG-EGFPGluA2(R683Q)	This paper	N/A
pRetroCAG-EGFPGluA2(R683E)	This paper	N/A
pRetroCAG-EGFPGluA2(813-862)	This paper	N/A
pRetroCAG-GFP	Tashiro et al., 2006	N/A
pCMV-gp	Tashiro et al., 2006	N/A
pCMV-vsv-g	Tashiro et al., 2006	N/A
Software and Algorithms		
ZEN Digital Imaging for Light Microscopy	Carl Zeiss	RRID:SCR_013672
ImageJ	National Institutes of Health	RRID:SCR_003070
IBM SPSS Statistics	IBM	RRID:SCR_002865
IGOR Pro	WaveMetrics, Inc	RRID:SCR_000325
Recording Artist (running under IgorPro)	Richard Gerkin, Arizona State University, USA	https://bitbucket.org/rgerkin/recording-artist
FBrain	Peter Jonas, Institute of Science and Technology, Austria	N/A
JCalc for Windows	Peter Barry, Sydney, Australia	N/A
BLASTn https://blast.ncbi.nlm.nih.gov/Blast.cgi?PROGRAM=blastn&PAGE_TYPE=BlastSearch&BLAST_SPEC=MicrobialGenomes&LINK_LOC=blasttab&LAST_PAGE=blastn	NIH/ NCBI	N/A
Other		
Quick Change II XL Site-Directed mutagenesis kit	Stratagene	N/A
Click-iT EdU Alexa Fluor 647 Imaging Kit	Thermo Fisher Scientific	Cat# C10340

CONTACT FOR REAGENT AND RESOURCE SHARING

Further information and requests for resources and reagents should be directed to and will be fulfilled by the Lead Contact, Maria Kukley (maria.kukley@uni-tuebingen.de).

EXPERIMENTAL MODEL AND SUBJECT DETAILS

Animals

NG2DsRedBAC transgenic mice (Ziskin et al., 2007) and C57BL/6 mice of both sexes were used in all experiments. Breeding pairs of NG2DsRedBAC transgenic mice were originally obtained from The Jackson Laboratory (stock 008241) and C57BL/6 mice were originally obtained from Charles River. Mice were bred in house and kept in 12-12 hours of light-dark cycle; food and water were available *ad libitum*. All experiments were performed in accordance with current European Union guidelines and approved by the local government authorities for Animal Care and Use (Regierungspraesidium Tuebingen, State of Baden-Wuerttemberg, Germany).

METHOD DETAILS

Molecular biology

pCI-EGFPGluA2(Q583) was a gift from Roberto Malinow (University of California, USA). The plasmids for viral production (pRetroCAG-GFP, pCMV-gp and pCMV-vsv-g) were gifts from Fred Gage (The Salk Institute, USA). The point mutation of GluA2(Q583) to GluA2(Q583E) was introduced using the Quick Change II XL Site-Directed mutagenesis kit (Stratagene). The primers for the point mutation were (5′ to 3′): fwd: CTTGGGTGCCTTTATGGAGCAGGGATGCGATATTTC and rev: GAAATATCGCAT CCCTGCTCCATAAAGG CACCCAAG. All the procedures followed the instruction manual provided by Stratagene. To construct pRetroCAG-GluA2(Q583)-GPF, pRetroCAG-GluA2(Q583E)-GFP and pRetroCAG-GluA2Ctail-GFP, we inserted GluA2(Q583)-GPF, GluA2(Q583E)-GFP and GluA2Ctail-GFP by PCR amplification. PCR primers included PmeI and AgeI restriction sites for insertion into pRetroCAG-GFP. For GluA2(Q583)-GPF and GluA2(Q583E)-GFP the primers were (5′ to 3′): forward TTACCGGTACGACTCACTATAGGCTAGAACTAG, reverse TGTTTAAACCCAAGGCCTGCATGCACTGCTTTG. For GluA2Ctail-GFP the primers were (5′ to 3′): forward TAGCGCTA CCGGTCGCCACCATGGTG, reverse TGGTTTAAACACCTCTACAAATGTGGTATGGCTG. The expression of all constructs was controlled by the chicken-beta actin (CAG) promoter. All plasmids were sequenced to ensure accuracy. For retroviral production, we used procedure described previously (Tashiro et al., 2006) with two modifications: we collected the supernatant 48 and 72 hours after transfection and filtered the supernatant through a 0.45 μm filter (Merck). The viral titers were 10^8-10^9/ml.

Experimental groups of animals

In the majority of experiments, the following 4 groups of animals were used: (1) Animals injected with retrovirus-GFP (called "GFP" throughout the manuscript); (2) Animals injected with retrovirus-GluA2(R583Q)-GPF (called "Ca^{2+}-permeable" throughout the manuscript); (3) Animals injected with retrovirus-GluA2(R583E)-GFP (called "pore-dead" throughout the manuscript); and (4) Animals injected with retrovirus-GluA2(813-862)-GFP (called "C-tail" throughout the manuscript). In some expetriments (see text), a fifth group of mice was used which contained naive animals, i.e., not injected with retrovirus (non-injected). The number of animals (*n*) used in each experiment is indicated in the corresponding figure legends.

Retrovirus injection

10-12 days-old NG2DsRedBAC transgenic mice were anesthetized with a mixture of isoflurane and oxygen (1%–3% v/v) and fixed in the stereotaxic frame (Stoelting, USA). The depth of the anesthesia was monitored by testing the reaction of the mouse to a toe pinch. For analgesia, metacam (1 mg/kg bodyweight, Boehringer Ingelheim) was injected subcutaneously before the surgery. The skin above the skull was disinfected, a small cut was made, and xylocaine (2%, Astra Zeneca) was applied locally. Bilateral injections of the virus into the corpus callosum were performed using the following coordinates (in mm from Bregma): anteroposterior 0.23, mediolateral ± 0.23-0.25, dorsoventral 1.77. For each injection we used a glass micropipette containing ∼2.5 μL viral stock solution. The micropipette was connected to a fast pressure application system (PDES-01D-4, NPI Electronic, Germany), and the following parameters were used for injection: pressure 16-20 psi, application duration 60-90 ms. Subsequently, the wound was sutured with silk (Ethicon, USA). After the surgery, mice recovered rapidly from anesthesia and were returned to their home cages with parents.

For electrophysiological experiments we used DsRed$^+$ mice of the NG2DsRedBAC line; for immunohistochemistry and cell counting we used DsRed$^-$ littermates in order to have the red fluorescent channel available for antibody labeling.

In vivo EdU treatment

To study cell proliferation, mice were administered with 5-ethynyl-2′-deoxyuridine (EdU, Thermo Fisher) (Young et al., 2013) intraperitoneally at a dose of 25 mg/ kg body weight. EdU was applied three times, i.e., on the third, fourth, and fifth day after the viral injection at an interval of 24 hours.

Slice preparation for electrophysiology

For patch-clamp recordings, we used in total 59 mice of the age P12-17. Three to five days after the viral injection mice were anesthetized with a mixture of isoflurane and oxygen (3% v/v) and decapitated. The brain was dissected in the ice-cold N-methyl-D-glucamine (NMDG)-based solution containing (in mM): 135 NMDG, 1 KCl, 1.2 KH_2PO_4, 20 choline bicarbonate, 10 glucose, 1.5 $MgCl_2$, and 0.5 $CaCl_2$ (pH 7.4, 310 mOsm), gassed with carbogen (95% O_2, 5% CO_2). 270-300 μm thick coronal brain slices were cut in the same solution using a Leica VT 1200S vibratome. The slices were transferred to a 32°C Haas-type interface incubation chamber and perfused with Ringer-solution containing (in mM): 124 NaCl, 3 KCl, 1.25 NaH_2PO_4*H_2O, 2 $MgCl_2$, 2 $CaCl_2$, 26 $NaHCO_3$, 10 glucose; 300 mOsm/kg; 7.4 pH; gassed with carbogen. The chamber was gradually cooled down to room temperature.

Patch-clamp recordings

At least one hour after the preparation, individual slices were transferred to a submerged recording chamber mounted on the stage of an up-right microscope (FN-1, Nikon, Japan) equipped with infrared differential interference contrast (IR-DIC) filters and a fluorescence light source. The slices were kept at room temperature and superfused continuously (~2 ml/min) with carbogenated Ringer solution. OPCs were selected for recordings based on fluorescence: red fluorescence (NG2DsRed$^+$ cells) for mice not injected with retrovirus, or green and red double-fluorescence (GFP$^+$NG2DsRed$^+$ cells) for mice injected with retrovirus. Patch pipettes were pulled from borosilicate glass capillaries (Science Products, Germany) on a vertical puller (Model PC10, Narishige, Japan). Pipettes had resistance of 4.8-7 MOhms when filled with K-gluconate-based internal solution containing (in mM): 125 K-gluconate, 2 Na_2ATP, 2 $MgCl_2$, 0.5 EGTA, 10 HEPES, 20 KCl, 3 NaCl; 280-290 mOsm/kg; titrated to pH 7.3 with KOH. Cells were voltage-clamped at a holding potential $V_h = -80$ mV with an EPC-8 amplifier (HEKA, Germany). The liquid junction potential was calculated using the software JPCalc for Windows (Peter H. Barry, Sydney, Australia) and V_h was corrected for a -13 mV liquid junction potential before seal formation. Series resistance was not compensated. After establishing the whole-cell configuration, ten depolarizing voltage steps (increment +10 mV) were applied to each cell from $V_h = -80$ mV, and corresponding current responses were recorded in order to verify that the selected cell was an OPC (Kukley et al., 2010). Evoked synaptic currents were elicited with an isolated pulse stimulator (A-M Systems, Model 2100, Science Products, Germany) using mono-polar glass electrode (resistance 5-6 MΩ) filled with Ringer solution and placed at 50-150 μm from the recorded cell ($V_h = -80$ mV). Paired (40 ms inter-pulse interval) monophasic rectangular pulses of 100-250 μsec duration were applied every 15 s. Trains of stimuli (20 pulses @ 100 Hz or 20 pulses @ 25 Hz) were applied each 15 s.

For I-V curve recordings, we used a Cs-based internal solution containing (in mM): 100 $CsCH_3SO_3H$ (CsMeS), 20 tetraethylammonium (TEA) chloride, 20 HEPES, 10 EGTA, 2 Na_2ATP, and 0.2 NaGTP; 280-290 mOsm/kg; titrated to pH 7.3 with CsOH, and a Ringer solution containing (in mM): 119 NaCl, 2.5 KCl, 1 NaH_2PO_4*H_2O, 1.3 $MgCl_2$, 2.5 $CaCl_2$, 26.2 $NaHCO_3$, 11 glucose; 300 mOsm/kg; 7.4 pH; gassed with carbogen. Spermine (Sigma, 100 μM) was included into the internal solution in all recordings of evoked EPSCs in order to test for the presence of Ca^{2+}-permeable AMPA receptors in OPCs. V_h was corrected for a -7 mV liquid junction potential before seal formation. The cells were held at different potentials (-90, -40, 0, $+20$, and $+40$ mV) and 10-15 sweeps were recorded at each potential.

When recording the synaptic currents, we applied a voltage step of -5 mV at the beginning of each sweep to monitor series resistance. Whole-cells currents in response to voltage steps were low-pass filtered at 10 kHz and digitized with a sampling frequency of 20 kHz (ITC-18, HEKA Instruments Inc, USA). All recordings of synaptic currents were low-pass filtered at 1 kHz and digitized with a sampling frequency of 10 kHz. Data acquisition was performed using Recording Artist (Rick Gerkin, Arizona State University, USA) running under Igor Pro 6.3 (WaveMetrics, Lake Oswego, USA). All recordings of evoked synaptic currents were performed in the presence of NMDA-receptor antagonist CPP (10 μM, Tocris) and GABA$_A$ receptor antagonist gabazine (5 μM, Sigma). In some experiments, TTX (0.5 μM, Abcam) or CNQX (10 μM, Abcam) was applied at the end of the recording. All drugs were dissolved in Ringer solution and applied via the bath. All patch-clamp recordings were performed at room temperature.

Immunohistochemistry

For MBP staining, C57BL/6 mice were sacrificed at P9, P10, P11, P12, P15, and P18. For all other stainings, mice were sacrificed 5 days after the retroviral injection. The brain was removed, and 350-400 μm thick coronal slices were cut using the Leica VT 1200S vibratome in the solution of the following composition (in mM): 87 NaCl, 2.5 KCl, 1.25 NaH_2PO_4*H_2O, 7 $MgCl_2$, 0.5 $CaCl_2$, 25 $NaHCO_3$, 25 glucose, 75 sucrose or NMDG-based solution. The slices were fixed overnight at 4°C in 4% paraformaldehyde, dissolved in 10 mM phosphate-saline buffer (PBS). Subsequently, thick slices were washed, embedded into Agar and re-sectioned in PBS to 30 μm thickness using a microtome (HM 650V, Thermo Scientific). All 30 μm thick slices were inspected visually for quality and for presence of GFP-expressing cells using an epi-fluorescence microscope (Axio Imager Z1m, Zeiss, Germany). Slices which did not contain green cells or appeared damaged were discarded. From the remaining pool, 4-12 slices per mouse were selected and used for immunohistochemistry and cell counting. The stainings were performed on 30 μm free floating slices in multi-well plates, or (in few cases) mounted on glass-slides. For antigen retrieval, the slices were incubated in 10 mM citric acid (pH = 6.0) at 37°C. After washing, we applied blocking solution containing: 0.1 M Tris-buffer saline (TBS), 3%–5% Albumin Fraction V (Roth), and 0.2%–0.5% Triton-X (Roth), at 37°C for 1 hour. Slices were incubated with primary antibody overnight in blocking solution. The following primary antibodies were used: rabbit or guinea pig anti-NG2 (1:500, gift from Bill Stallcup, Burnham Institute, La Jolla, USA), mouse anti-APC (1:250, Ab-7, CC-Calbiochem), rabbit anti-Cleaved-Caspase-3 (1:500, Cell Signaling Technology), chicken anti-GFP (1:500, Abcam),

rat anti-MBP (1:125, Abcam), mouse anti-ki67 (1:500, BD PharMingen), mouse anti-MAG (1:1000 Santa Cruz Biotechnology). Detection was performed using the following secondary antibodies: goat anti-rabbit Alexa Fluor 568 (1:500, Invitrogen), goat anti-rabbit Cy5 (1:500, Dianova), goat anti-rabbit Alexa Fluor 405 (1:150, Invitrogen), goat anti-guinea pig Alexa Fluor 633 (1:500, Invitrogen), goat anti-mouse Alexa Fluor 555 (1:500, Invitrogen), donkey anti-chicken FITC (1:1000, Dianova), goat anti-chicken Alexa Fluor 488 (1:500, Invitrogen) or goat anti-rat biotin-SP (1:200, Dianova) followed by streptavidin-Cy3 (1:200, Dianova). Secondary antibodies were applied for 3 hours at 37°C. For EdU visualization, the protocol recommended by Thermo Fisher Scientific was used. Diamidino-2-phenylindole dihydrochloride (DAPI, 0.2 μg, Sigma) was used for counterstaining of the cell nuclei.

Image acquisition

A confocal LSM 710 system (Zeiss, Germany) was used for image acquisition. Images containing corpus callosum were acquired and saved as z stacks with 16 bit pixel depth. Each z stack was 6-18 μm thick and consisted of 6-18 z-slices at a step size of 1 μm. Each layer of a z stack was acquired as a tile-scan (vertical x horizontal: 3 × 7 or 2 × 7 images), where each tile was 512 × 512 pixels in size. Pixel size was usually 0.415 × 0.415 μm, with exception of images shown in Figures S3B and S3C, where pixel size was 0.033 × 0.033 μm. Each tile-scan represented a quadruple-channel fluorescence image, where channels were acquired sequentially in ZEN software using 40x oil-immersion objective (NA = 1.3). For images shown in Figures S3B and S3C we used 63x objective (NA = 1.4). The following excitation laser lines and emission detection ranges were used: for DAPI excitation 405 nm, emission 414-490 nm; for FITC excitation 488 nm, emission 497-556 nm; for Alexa-555, Alexa-568 or Cy3 excitation 561 nm, emission 569-633 nm; for Alexa-633 or Alexa-647 excitation 633 nm, emission 650-740 nm. The beam splitters for each dye matched the excitation laser lines. The pinhole was set to 1.07-1.42 airy units and adjusted such that the optical section for each channel was 1.2 μm. The exception are the images shown in Figure 1C, where we used 10x objective and optical section was 12.3 μm. Laser power, detector gain, and offset were adjusted such that in the final scan (average of 2 frames) a good signal to background noise ratio was achieved. For visualization, images presented in the figures were adjusted for brightness/contrast in ImageJ (NIH, USA), as follows: Figure 1F, brightness of GFP staining; Figure 1I, brightness and contrast for NG2 and CC1 staining; Figure 1J, brightness and contrast for CC1; Figure 3B, brightness and contrast for NG2 and CC1 staining for pre-OL; Figure 3H, brightness for NG2 staining; Figure 3J, brightness and contrast for GFP staining; Figure 4B, brightness of EdU staining for GFP group; Figure 4F, brightness for GFP staining in GFP group; Figure S2E, brightness for GFP; Figure S2F, brightness for GFP; Figures S3B and S3C, brightness and contrast for GFP (green; without antibody labeling) and GFP staining (red; non-permeabilized conditions); Figure S3G, brightness and contrast for Caspase3.

QUANTIFICATION AND STATISTICAL ANALYSIS

Analysis of electrophysiology data

Only recordings where the offset drift by the end of the experiment was smaller than ± 5 mV, and the change of the series resistance was < 30% relative to the original value were considered for the analysis. The series resistance was between 20 and 40 MΩ.

Analysis of evoked EPSCs, I-V curve, and paired-pulse ratio

Analysis of evoked EPSCs was performed using custom-written macros in IgorPro. Stimulus artifacts were removed using the following procedure: sweeps containing failures (absence of postsynaptic response) after the first stimulus, or sweeps recorded in the presence of TTX or CNQX, were averaged and the segment of the averaged sweep from time-point of stimulation to last point before the second stimulus was cut out, duplicated and concatenated with itself. The resulting sweep was subtracted from each recorded sweep.

To measure the EPSC amplitude (after first or second pulse), we used the following procedure: For each recorded sweep the baseline was adjusted to the 100-ms segment immediately preceding the stimulation; the peak-center of each event was determined as the time-point at which the first derivative of the sweep crossed zero; the amplitude values of the current in the peak-center and in 4 points around it (2 points to the right and 2 points to the left) were averaged, and the resulting value was taken as current amplitude. The threshold for event detection was determined individually for each recorded sweep and was equal to three times the standard deviation of the noise. In case several EPSCs occurred after a given stimulus, care was taken to measure the amplitude of the first event.

Although we used paired-pulse stimulation in all experiments, in order to generate the I-V curve we considered only the EPSCs occurring after the first pulse. The amplitudes of all recorded sweeps (10 to 15) at a given holding potential (−90, −40, 0, +20, +40 mV, and back to −90 mV) were measured as described above, and averaged. The resulting averages were used to generate the I-V curve in each cell. To calculate the rectification index, the average value of the EPSC amplitude at +40 mV was divided by the average value of the EPSC amplitude at −90 mV.

To determine the paired-pulse ratio, the average amplitude value of the EPSC occurring after the second pulse was divided by the average amplitude value of the EPSC occurring after the first pulse at a holding potential of −90 mV.

Analysis of delayed EPSCs

To study the quantal amplitude of synaptic currents in OPCs, we analyzed the delayed EPSCs occurring in OPCs after the train stimulation of callosal axons with 20 pulses at 25 or 100 Hz. The delayed EPSCs were defined as those with an onset of > 10 ms after the last stimulus of the train. In each recorded cell we collected the delayed EPSCs in 20-160 sweeps of 1.73-2.3 s length each. The EPSCs were detected using a deconvolution-based algorithm (Pernía-Andrade et al., 2012) in FBrain, a customized program running

under IgorPro 6 (WaveMetrics, Lake Oswego, USA). FBrain was kindly provided by Peter Jonas Lab (IST, Klosterneuburg, Austria). Additional digital high-pass (10 Hz) and Notch (50 ± 0.5 Hz) filtering was applied to the recorded sweeps in FBrain before the analysis. The deconvolution trace was passed through a digital band-pass filter at 0.001 to 200 Hz. The event detection template had a rise-time of 0.5 ms, a decay time constant of 4 ms, and amplitude of -3 pA. The event detection threshold (θ) was set to 4.2 times the standard deviation of a Gaussian function fitted to the all-point histogram of the deconvolved trace (Pernía-Andrade et al., 2012). All events detected by the algorithm were inspected visually, and those events which clearly did not show kinetics of typical excitatory postsynaptic currents (i.e., fast rise and exponential decay) were manually removed. The subsequent analysis was performed using custom-written macros in IgorPro.

Cumulative probability histogram of the amplitude of delayed EPSCs
The following procedure was used: (1) The amplitude of all delayed EPSCs was measured in each cell as described above; (2) 67 delayed EPSCs were randomly selected from each cell using the StatsSample procedure in IgorPro; (3) the amplitude distribution of randomly selected events was compared to the amplitude distribution of all events within a given cell using the Kolmogorov-Smirnov test in IgorPro to ensure that the two distributions were similar, and the pool of randomly selected events was representative of the whole population of events. In case the two distributions were different, the random selection was automatically repeated until no difference was found between the distributions; (4) in each cell, steps (2)-(3) were repeated 100 times; (5) for each of the 100 trials, the randomly selected events from all cells within a given experimental group were pooled to generate an EPSCs amplitude distribution per experimental group; (6) for each of the 100 trials this new amplitude distribution of the events in a group of animals expressing one of the GluA2-subunit modifying constructs was compared to the GFP group using the Kolmogorov-Smirnov test in IgorPro. In selected trials, the comparison was repeated using SPSS.

For data presentation in Figure 2H and Figure S1E, we chose one representative example from the 100 random selection trials for each experimental group. The bin size for cumulative probability histograms was 0.5 pA, and each histogram was normalized to probability density using built-in function in IgorPro.

Non-stationary fluctuation analysis (NSFA)
To estimate the single channel conductance of synaptic AMPARs in OPCs we performed peak-scaled non-stationary fluctuation analysis (Hartveit and Veruki, 2007). In each cell, the delayed EPSCs were examined visually and only the events with smooth rise- or decay phase were selected for NSFA. Spearman's rank-order correlation test was applied to verify that there was no drift in the peak amplitude, rise-time, or decay-time of the events during the time-course of each experiment. In addition, we also verified that there was no correlation between rise-time and decay-time constant (Hartveit and Veruki, 2007). If any of the indicated correlations was found, the cell was excluded from the NSFA. On average, 13 events (range 7-17) were selected randomly from each cell (n = 6 cells for GFP, n = 5 for "Ca^{2+}-permeable," n = 7 cells for "pore-dead," and n = 8 for "C-tail"), and were pooled within each experimental group. This resulted in, on average, 82 events (range 57-94) included into the NSFA within each experimental group. The events were aligned on the point of steepest rise, which corresponds to the location of the minimum value of the first time derivative of the event waveform. The mean waveform was calculated from these events and the amplitude of the mean waveform was scaled to the amplitude of each individual event. Subsequently, the scaled mean waveform was subtracted from each individual event, resulting in the noise component for each event, from which the variance was calculated. The background variance was estimated from the segment of the trace before the onset of each event, and was subtracted. The ensemble background-subtracted variance was calculated as an average of variances of all events. The mean amplitude wave was binned into 18 bins, and the corresponding values of the variance wave were then obtained in accordance with this binning (Hartveit and Veruki, 2007). Different number of bins was also tested, but varying the number of bins did not affect the results. Finally, the values of variance were plotted versus the corresponding values of the mean current amplitude. The resulting variance-mean relationship was fitted with the following parabola function in IgorPro:

$$\delta^2(I) = i * I - I^2 / N + \delta_{bgr}^2$$

where $\delta^2(I)$ is the variance; i is the (weighted) estimate of a mean single channel current; N is average number of channels opened at the peak, and δ_{bgr}^2 is the background variance. The single-channel conductance (γ) of synaptic AMPAR was calculated from the single-channel current i as:

$$\gamma = i/E$$

where E is the driving force for AMPAR-mediated EPSC, which is -80 mV in our study.

Notably, because we used the peak-scaling method for NSFA, the information on the total number of available channels is lost (Hartveit and Veruki, 2007), the parameter N has no meaning, and is not further analyzed/presented in our study.

The random selection, the pooling process, and all subsequent procedures described above were repeated 100 times for each of our 4 experimental groups, and by 4 researchers, resulting in total of 400 random selections and pooling per experimental group.

All routines for NSFA were custom programmed and were based on the code presented in the supplementary material of Hartveit and Veruki (Hartveit and Veruki, 2007).

Estimation of the fraction of rectifying AMPARs (FRR) based on rectification measurements

To obtain the FFR, we used the equation developed by Stubblefield and Benke (Stubblefield and Benke, 2010), which allows for estimation of the FRR based on rectification measurements. Their rectification indices were calculated as a ratio of EPSC amplitudes recorded at -70 mV and at $+40$ mV. To match their approach, we took the inverse of our *RI* values (*1/RI*) from Figure 2E and adjusted their equation to model our results as follows:

$$FFR = (1 - 1/RI * F3)/1/RI * (F1 - F3),$$

where *F1* is the maximal block of inwardly rectifying receptors (EPSC at $+40$ mV/ EPSC at -90mV), extrapolated to be 0.035 (based on (Rozov et al., 1998; Stubblefield and Benke, 2010)). *F3* is the value for linear relationship (F3 = 40/90 = 0.444). This analysis assumes that there is no change in presynaptic function (c.f. Figures S1F and S1G and Figures S3D–S3E).

Cell counting

We counted GFP-labeled infected cells in z stack images using ImageJ Cell Counter plugin (NIH, USA). No contrast or brightness adjustment was made in any of the images, but background subtraction was applied to the green channel before counting. The background fluorescence was measured using the linear 'plot profile' function in ImageJ and the resulting value was subtracted from each pixel of the original image. The ventral and dorsal borders of corpus callosum were identified based on the CC1 or NG2 and DAPI staining. For counting, in each coronal slice we outlined the area of the corpus callosum approximately 500-850 μm laterally on each side from the midline. Thus, the ROI spanned 1-1.4 mm along the mediolateral axis of the corpus callosum and avoided cells in the vicinity of lateral ventricles. Only cells within the ROI and cells whose nucleus was $\geq$ 50% within its borders were included in the analysis. Cells were counted in 4-12 slices from each mouse and the counts within one animal were summed, resulting in 29 to 486 GFP$^+$ cells per animal. OPCs were identified as GFP$^+$NG2$^+$CC1$^-$ cells, pre-myelinating oligodendrocytes as GFP$^+$NG2$^+$CC1$^+$ cells, and myelinating oligodendrocytes as GFP$^+$NG2$^-$CC$^+$ cells. To avoid bias, in randomly selected experiments the counting was repeated by one or two additional investigators blind to the experimental group of animals. The differences in counts were minor and did not affect the final results.

Statistics

All data acquisition was randomized (animals for viral injections, cells during patch-clamp experiments). Throughout the study we made all efforts to avoid pseudoreplications, both when performing experiments in slices and *in vivo*. The exact number of cells and animals used in each experiment is given in the figure legends.

Statistical analysis was performed using SPSS, including tests for homoscedasticity and normal distribution. If the datasets had normal distributions and equal variances, one-way ANOVA with post hoc Dunnett's or Bonferroni (Figures 3E–3G) test was used. If the datasets had normal distributions but unequal variances, one-way ANOVA with post hoc Games-Howell test was used. If the datasets were not normally distributed, Kruskal-Wallis with post hoc Dunn's test was used. In all Figures, except the Figures 3E–3G, we were interested only in the comparison between the experimental groups with AMPAR-manipulation and the GFP control group. Therefore, the *p* values in the Figure Legends are shown only for these comparisons. To compare values of rectification index and paired-pulse ratio between cells in non-injected and GFP expressing animals, we tested the datasets for normal distribution and used the 2-tailed Student's t test. To compare cumulative probability histograms of the amplitude of the delayed EPSCs between control (GFP) and each experimental group ("Ca^{2+}-permeable," "pore-dead," or "C-tail"), 100 trials of random selections of events were performed and compared in IgorPro with Kolmogorov-Smirnov test as described above. Comparison of the GFP and "Ca^{2+}-permeable" groups showed that the two distributions were different in all 100 trials therefore, we considered the difference between these two distributions statistically significant. Comparison of the GFP and "pore-dead" groups showed that the two distributions were different in 98 out of 100 trials therefore, we considered the difference between these two distributions statistically significant. Comparison of the GFP and "C-tail" groups showed that the two distributions were different in only 46 out of 100 trials; therefore, we considered the difference between these two distributions not statistically significant. To report the corresponding p values in the figure, we used the Kolmogorov-Smirnov test in SPSS. For all statistical comparisons, significance level was set at p < 0.05. Statistically significant differences are indicated by *p* values in the figure legends. * represents p $\leq$ 0.05, ** represents p $\leq$ 0.01, and *** represents p $\leq$ 0.001. For graphs, each point represents an individual data point (cell or animal) and the diamond represents the mean $\pm$ SEM. Data in the text report mean $\pm$ SEM.

DATA AND SOFTWARE AVAILABILITY

The datasets generated and analyzed in the current study and custom-written macros for electrophysiological analysis are available from the lead author upon request.